PNAS RESEARCH ARTICLE | CHEMISTRY

Uncoordinated chemistry enables highly conductive and stable electrolyte/filler interfaces for solid-state lithium–sulfur batteries

Yanfei Zhu[a,b,1], Qi Zhang[a,1], Yun Zheng[b,1], Gaoran Li[b], Rui Gao[b], Zhihong Piao[a], Dan Luo[b], Run-Hua Gao[a], Mengtian Zhang[a], Xiao Xiao[a], Chuang Li[a], Zhoujie Lao[a], Jian Wang[c], Zhongwei Chen[b,2], and Guangmin Zhou[a,2]

Edited by Alexis Bell, University of California, Berkeley, CA; received January 5, 2023; accepted February 17, 2023

Composite-polymer-electrolytes (CPEs) embedded with advanced filler materials offer great promise for fast and preferential Li^+ conduction. The filler surface chemistry determines the interaction with electrolyte molecules and thus critically regulates the Li^+ behaviors at the interfaces. Herein, we probe into the role of electrolyte/filler interfaces (EFI) in CPEs and promote Li^+ conduction by introducing an unsaturated coordination Prussian blue analog (UCPBA) filler. Combining scanning transmission X-ray microscope stack imaging studies and first-principle calculations, fast Li^+ conduction is revealed only achievable at a chemically stable EFI, which can be established by the unsaturated Co–O coordination in UCPBA to circumvent the side reactions. Moreover, the as-exposed Lewis-acid metal centers in UCPBA efficiently attract the Lewis-base anions of Li salts, which facilitates the Li^+ disassociation and enhances its transference number (t_{Li}^+). Attributed to these superiorities, the obtained CPEs realize high room-temperature ionic conductivity up to 0.36 mS cm^{-1} and t_{Li}^+ of 0.6, enabling an excellent cyclability of lithium metal electrodes over 4,000 h as well as remarkable capacity retention of 97.6% over 180 cycles at 0.5 C for solid-state lithium–sulfur batteries. This work highlights the crucial role of EFI chemistry in developing highly conductive CPEs and high-performance solid-state batteries.

composite polymer electrolytes | electrolyte/filler interfaces | metal–organic frameworks | ligand modification | solid-state lithium–sulfur batteries

Lithium-sulfur batteries (LSBs) combined with solid-state electrolytes (SSEs) have attracted enormous attention because of their high safety and low cost (1, 2). Among various SSEs, solid polymer electrolytes (SPEs) hold great promise owing to their significant advantages over solid inorganic electrolytes including lightweight, easy processability, high flexibility, and particularly compatible electrode–electrolyte interfaces in solid-state LSBs (3). However, the implementation of SPEs is still hindered by the low room-temperature (RT) ionic conductivity and Li^+ transference number (t_{Li}^+) (4).

Composite polymer electrolytes (CPEs) with filler offer considerable opportunities to tackle the Li^+ kinetic issue of SPEs. CPEs contain three parts including polymer electrolyte matrix, fillers, and their interfacial regions. While the mechanism of ionic migration in the polymer electrolyte matrix is similar to that in SPEs (5), where Li^+ hops in the amorphous regions, the overall kinetics of Li^+ conduction in CPEs can be improved for the following reasons: (i) The fillers modify the local structure of polymer chains and decrease their crystallinity, (ii) the fillers help further dissociate Li salts based on Lewis acid–base theory, and (iii) the fillers can act as ion "accelerator" by forming cross-linking clusters at the electrolyte/filler interface (EFI) regions (6). However, the addition of fillers does not always effectively improve the properties of CPEs. According to the published literature, promoting the effect of fillers in CPEs is distinguishing, and even the same kind of filler in the systems with different polymer electrolyte matrixes has an extreme disparity (7). A compatible EFI can decouple cations (e.g., Li^+ from Li salts) and provide consecutive transport channels for accelerated ion hopping through stable and efficient interfacial contact layers. However, if the filler is chemically unstable or incompatible when coexisted with Li salts, the interface could be ineffective or even broken to impede ionic migration (8–10). Therefore, a more fundamental understanding of interfacial chemistry at the EFI in CPEs is urgently needed.

In order to gain deep insight into the EFI in CPEs, we chose metal–organic frameworks with tunable chemical structures and characteristics as fillers. Their extraordinarily high surface area also benefits the sufficient interfacial contact with other components especially the anions of Li salts (11). In addition, their surface polarity ascribed to the controllable active metal sites enables the modulation of Lewis acid–base interactions in the hybrid systems, which provides possibilities for the optimization of overall electrochemical properties (12–14).

Significance

To boost the application potential of solid-state batteries, developing composite polymer electrolytes (CPEs) with filler embedded is a promising way yet challenging. A major concern is limited interfacial stability between the polymer electrolyte and filler, leading to disparity in different CPEs, especially because of our restricted understanding. Therefore, a fundamental insight of interface chemistry at the electrolyte/filler interfaces (EFI) is urgently needed. We overcome this limitation using uncoordinated chemistry strategy that accurately constructs a coordinatively unsaturated metal-organic frameworks filler for improving the compatibility of EFI. More broadly, we probed into the role of EFI in CPEs via scanning transmission X-ray microscope stack imaging technique and revealed that the high-efficiency Li^+ conduction is only achievable at a chemically stable EFI.

Author contributions: Y. Zhu, M.Z., and G.Z. designed research; Y. Zhu, Q.Z., Y. Zheng, G.L., R.G., M.Z., C.L., and J.W. performed research; Y. Zhu, Q.Z., G.L., Z.P., D.L., R.-H.G., M.Z., X.X., C.L., Z.L., J.W., Z.C., and G.Z. analyzed data; and Y. Zhu and G.Z. wrote the paper.

The authors declare no competing interest.

This article is a PNAS Direct Submission.

[1]Y. Zhu, Q.Z. and Y. Zheng contributed equally to this work.

[2]To whom correspondence may be addressed. Email: zhwchen@uwaterloo.ca or guangminzhou@sz.tsinghua.edu.cn.

This article contains supporting information online at https://www.pnas.org/lookup/suppl/doi:10.1073/pnas.2300197120/-/DCSupplemental.

Published April 5, 2023.

In this work, Prussian blue analog (PBA) fillers $Co_3[Co(CN)_6]_2 \cdot 12H_2O$ with and without Co–O ligand modification, namely unsaturated coordination PBA (UCPBA) and saturated coordination PBA (SCPBA), respectively, are used as fillers in poly(vinylidene fluoride-co-hexafluoropropylene) (PVDF-HFP) polymer matrix (15). According to the results of scanning transmission X-ray microscope (STXM) stack imaging, we found that the compatibility between fillers and polymer electrolyte matrix is a critical factor in determining the overall performance of CPEs. UCPBA with coordinative unsaturation has moderate host–guest interactions with Li salt in the polymer electrolyte matrix, providing a stable and efficient EFI. The compatible EFI further facilitates the cation disassociation and improves its migration through the interfacial regions. On the contrary, SCPBA has poor interfacial chemical stability against Li salt, which leads to an incompatible EFI and thus exhibited an interruption of cation migration. As a result, the UCPBA-modified CPE displayed a superior RT ionic conductivity of 0.36 mS cm^{-1} (≈12 times that of SCPBA-based CPE) and a high t_{Li^+} of 0.6. In addition, the mechanical strength and long-term stability of the UCPBA-modified CPE were also improved so that it cycled for over 4,000 h in Li//Li cells and demonstrated a high capacity retention of 97.6% at 0.5 C in Li//sulfurized polyacrylonitrile (Li//SPAN) cells.

Results and Discussion

The $Co_3[Co(CN)_6]_2 \cdot 12H_2O$ consists of three kinds of metal cobalt including inner Co coordinated with O and surface Co coordinated with C or N and C≡N ligands to sustain a three-dimensional coordinated framework (Fig. 1*A*) (16, 17). Specially, the Co–O ligands formed and located at the defect sites inside the subunit of the single crystal lattice are in a saturated coordination state. To obtain UCPBA filler, SCPBA was first collected through coprecipitation of cobalt(II) acetate tetrahydrate $[Co(CH_3COO)_2 \cdot 4H_2O]$ and potassium hexacyanocobaltate(III) $(K_3[Co(CN)_6])$ in a water solution, followed by thermal treatment under vacuum conditions (details in *SI Appendix*) (18, 19). Both the as-obtained SCPBA and UCPBA present well-defined nanocube morphology with diameters of ~500 nm explored by scanning electron microscope (SEM) (Fig. 1 *B* and *C*). Through the physical dehydration, Co–O ligands were broken accompanied by the release of water molecules, and the sample color changed from pink to blue (20). It can be perceived from attenuated total reflectance-Fourier transform infrared (ATR-FTIR) spectra that the O–H modes at around 3,500 cm^{-1} and 1,600 cm^{-1} are sharply weakened in UCPBA compared with SCPBA (*SI Appendix*, Fig. S1). Besides, the decreased vibration intensity of Co–O mode at around 700 cm^{-1} indicates the efficient dehydration process. The crystalline phases of SCPBA and UCPBA were analyzed by powder X-ray diffraction (XRD), where both patterns can be indexed to the standard diffraction pattern of the $Co_3[Co(CN)_6]_2 \cdot 12H_2O$ (JCPDS No. 77-1161) (*SI Appendix*, Fig. S2) (21). This result signified that the Co–O ligands modification process has little influence on the long-range ordered structures of samples. Based on these findings, the normalized Co K-edge X-ray absorption spectra (XAS) were collected to probe the potential transitions in the local structure and chemical environment. As shown in Fig. 1*D*, the X-ray absorption near-edge structure (XANES) witnesses two pre-edge features assigned to 1s → 3d transition at 7,695 eV and 7,697 eV for both samples, whereas an increase in intensity after dehydration suggests the transition feature from the initial complete octahedral geometry to a partially low-order symmetric geometry of Co clusters (22). An obvious uplift of UCPBA at 7,700 to 7,705 eV relative to SCPBA further illustrates the lattice distortion that occurred during Co–O ligands modification process, accompanied by decreased intensity of the white line (23). In addition, the E_0 in 1st derivative of the energy edge in both samples is identical, which indicates unchanged valence states of Co in the bulk environment (*SI Appendix*, Fig. S3). The corresponding k^3-weighted Fourier transform of extended X-ray absorption fine structure (EXAFS) was analyzed as shown in Fig. 1*E*. The first and second coordinated shells are assigned to the Co–C/N and Co–O scattering paths, respectively (24). Notably, the relatively weaker intensity of Co–O oscillation in UCPBA reveals its more disordered local structure as well as less coordination around Co–O sites. Wavelet transform (WT) is used to further analyze Co K-edge EXAFS oscillations (*SI Appendix*, Fig. S4). The WT contour plots of SCPBA exhibit an intensity maximum at 11 $Å^{-1}$ between 1 Å and 2 Å, which can be assigned to the coordination of Co with adjacent C, N, and O. In contrast, the almost missing intensity maximum and lower corresponding k value of 8 $Å^{-1}$ in WT plots of UCPBA represent the reduction of Co–O oscillation. Subsequently, the total coordination number extracted from quantitative EXAFS fittings decreases from a nearly saturated coordination number of 5.9 to 4.8 after dehydration, strongly validating the coordinative unsaturation of the Co sites in UCPBA (*SI Appendix*, Table S1) (25).

For further understanding of the influence of Co–O ligand unsaturation on local interfacial chemistry especially when combined with Li salt, the STXM stack imaging and Co L-edge extracted near-edge X-ray absorption fine structure (NEXAFS) spectra of SCPBA@lithium bis(trifluoromethanesulfonyl)imide (LiTFSI) and UCPBA@LiTFSI composites were investigated (Fig. 1 *F* and *G*) (26–29). Stack analyses were first applied to Co spatial distributing region and presented as a color-coded map (pink, green, and red). Both the two composites show homogeneous Co distribution from the outer layer (pink region) to the inner (red region) with similar optical density. NEXAFS spectra extracted from the color-coded map exhibit a mixture of characteristic peaks of Co^{2+} and Co^{3+}. In terms of SCPBA@LiTFSI, the peaks located at 779.0 eV and 779.7 eV can be assigned to Co^{2+} combined with O (originated from H_2O in SCPBA) or N, while the peak located at 782.7 eV is associated with the Co^{3+}–C coordination (Fig. 1*F*) (30). In particular, the tiny shoulder peak that emerges at 778.3 eV only shown in the outer layer can be assigned to Co–O (O is originated from TFSI anion) coordination, indicating an undesired side-reaction between SCPBA and LiTFSI. This is also confirmed by the narrower peak width of the outer layer compared with the middle and inner layers. In contrast, the spectra of UCPBA@LiTFSI remain consistent from outer to inner layers, proving that the UCPBA can afford moderate but stable interfacial compatibility when exposed to LiTFSI, which is further evaluated by subsequent density functional theory (DFT) calculations (Fig. 1*G*). The optimized configurations of SCPBA (001) and UCPBA (001) obtained from DFT calculations are shown in *SI Appendix*, Fig. S5. The stable configurations illustrate that the local ligand modification process maintains the crystal structure, which is consistent with the previous XRD results. Moreover, the smaller bond lengths of Co–C, Co–N, and Co–O in UCPBA indicate a more compact geometry configuration, which makes UCPBA more crystallographically stable compared with SCPBA (*SI Appendix*, Table S2). When LiTFSI interacts with SCPBA, the bond lengths of Co–C, Co–N, and Co–O are increased, which induces the configuration collapse where the upper layer tightly combined with LiTFSI is broken down and separated from the bottom layer, leading to a chemically unstable EFI (*SI Appendix*, Fig. S6). By contrast, when LiTFSI adsorbs on the UCPBA surface, the system maintains integrity with high thermodynamical

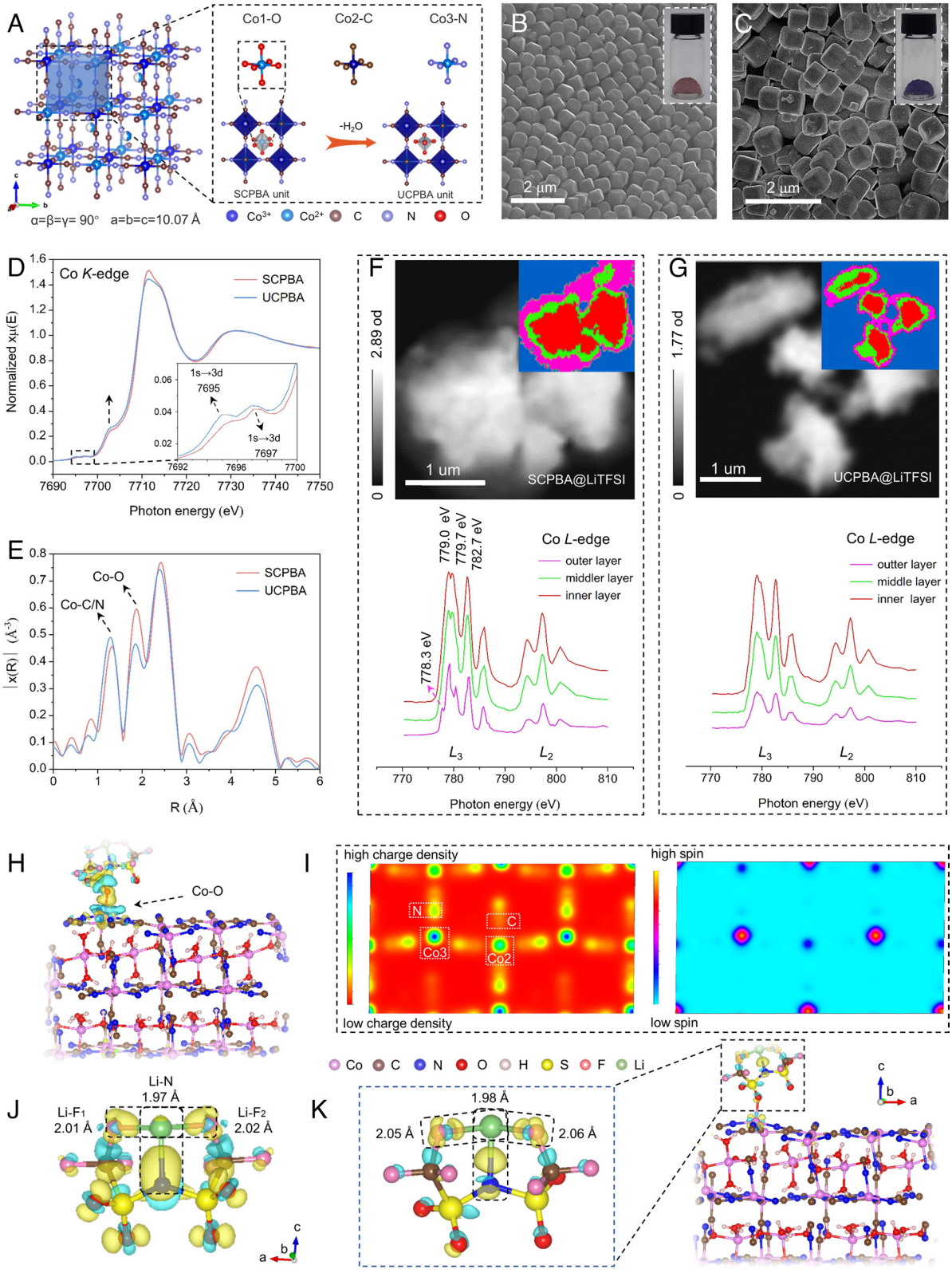

Fig. 1. Intrinsic properties and characteristics of the SCPBA and UCPBA. (*A*) A crystal structure unit cell of SCPBA. (*B* and *C*) SEM images of (*B*) SCPBA and (*C*) UCPBA, *Insets* are the physical and color states of samples at RT. (*D* and *E*) Co *K*-edge XANES (*D*) and Fourier transform EXAFS spectra (*E*) of SCPBA and UCPBA. (*F* and *G*) Co *L*-edge STXM imaging stack and corresponding NEXAFS spectra of (*F*) SCPBA@LiTFSI and (*G*) UCPBA@LiTFSI composites. (*H*) Stable geometrical configurations of LiTFSI on (001) surface of UCPBA. (*I*) Intrinsic charge densities and spin states of Co, C, and N in UCPBA. (*J* and *K*) Change of coordination bond length in (*J*) single LiTFSI molecular and (*K*) UCBPA adsorbed LiTFSI.

stability through the coupling of the O atom in LiTFSI with Co (Fig. 1*H*). In detail, the LiTFSI prefers to adsorb on the Co–N site instead of Co–C (*SI Appendix*, Figs. S7 and S8), due to the intrinsic high spin and charge density of Co^{2+} (Fig. 1*I*) (31). Moreover, the interaction between UCPBA and LiTFSI weakens the electron coupling effect of Li^{+} and $TFSI^{-}$, resulting in increased

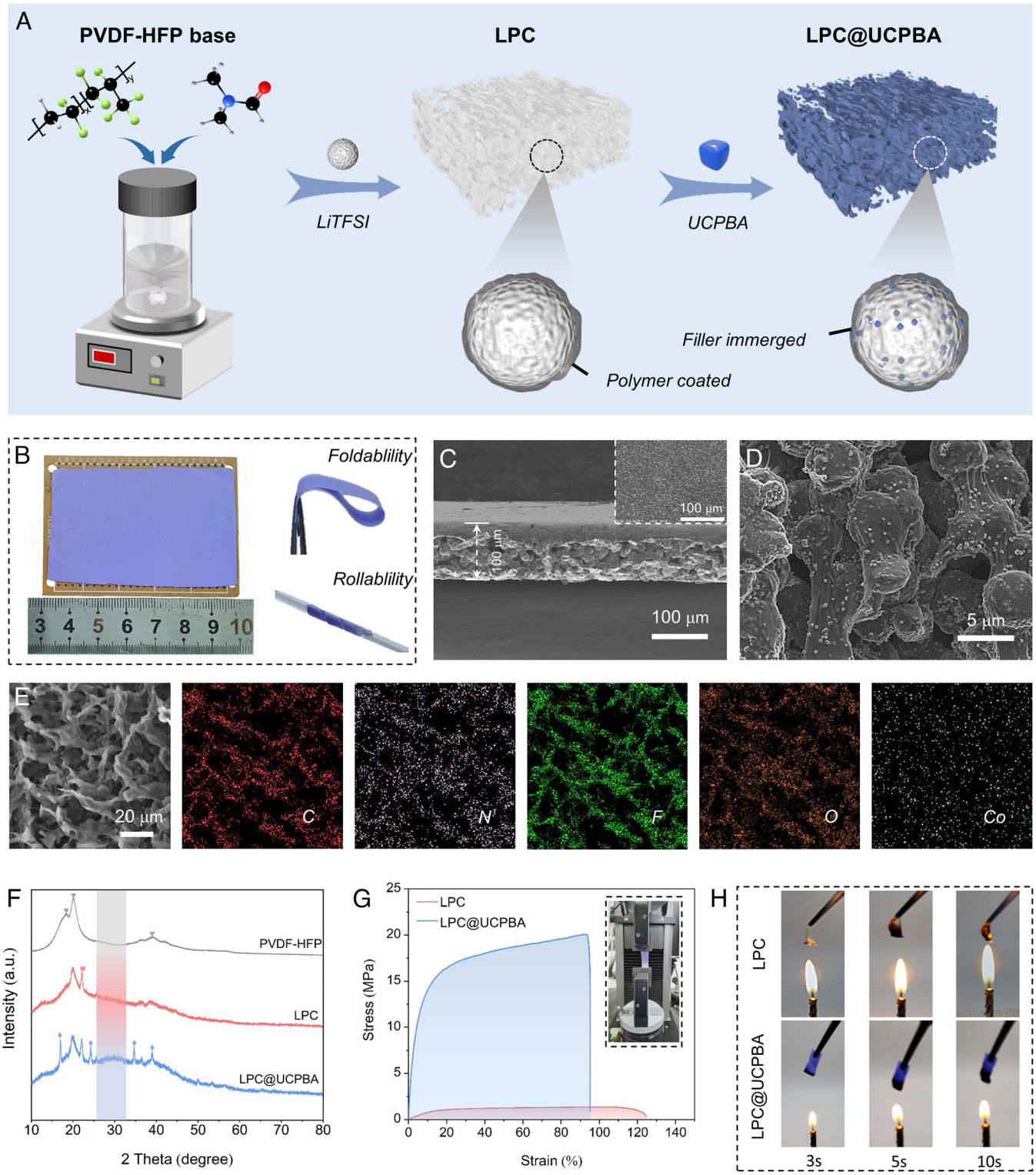

Fig. 2. Preparation and characterization of the LPC and LPC@UCPBA membrane electrolytes. (*A*) Illustration of the preparation process of LPC and LPC@UCPBA. (*B*) Optical photographs of LPC@UCPBA in the plane, folding, and rolling states. (*C* and *D*) Cross-sectional SEM images of LPC@UCPBA at different magnifications (*Top*-view plot shown in the *Inset*). (*E*) EDX maps of LPC@UCPBA. (*F*) XRD patterns of PVDF-HFP, LPC, and LPC@UCPBA membranes. The gray triangles, red heart, and blue rhombus are assigned to crystal PVDF-HFP, LiTFSI, and UCPBA, respectively. (*G*) Tensile modulus of elasticity of LPC and LPC@UCPBA membranes. (*H*) Flammability tests of LPC and LPC@UCPBA membranes.

bond lengths of Li–N and Li–F (Fig. 1 *J* and *K* and *SI Appendix*, Table S3). Therefore, the combined effect between the unsaturated coordination of UCPBA and the intermolecular dipole interaction between Co^{2+} and LiTFSI contributes to a faster Li^{+} association/relaxation.

The fabrication process of electrolyte membranes consisting of an equal mass ratio of LiTFSI and PVDF-HFP composite (LPC) with UCPBA (LPC@UCPBA) is shown in Fig. 2*A*. The LPC@UCPBA membranes exhibit flexible and malleable properties under severe bending (Fig. 2*B*). Similarly, pure PVDF-HFP and

LPC membranes without any fillers were also fabricated for comparison (*SI Appendix*, Fig. S9). To show the microstructure morphology and the distribution of LiTFSI, polymer, and fillers, SEM images of membranes in the view of plane and cross-section are presented. The pure PVDF-HFP membrane displays a porous configuration for intrinsic structural support to associate with the immerged LiTFSI particles (*SI Appendix*, Fig. S10). As shown in Fig. 2*C*, the thickness of the LPC@UCPBA membrane is ~100 μm. In addition, the smooth surface of the membrane is free of notable cracks or voids (*Inset* of Fig. 2*C*), and LiTFSI particles are uniformly dispersed in the cross-linked PVDF-HFP matrix. Meanwhile, the magnified SEM image in Fig. 2*D* reveals the homogeneous distribution of UCPBA fillers in the whole CPE system, which is further confirmed by the corresponding EDX mapping images shown in Fig. 2*E*. Based on all aspects of information, the close-grained packing, as well as robust contact between the fillers and polymer electrolyte, affords a consecutive network that can achieve effective conductive pathways, which ensures fast Li^+ hopping through the stable EFI in the LPC@UCPBA membrane. The phases and crystallinity of these membranes were characterized by XRD, as shown in Fig. 2*F*. The pure PVDF-HFP exhibits characteristic peaks at 18°, 20°, and 40°, which correspond to (100), (020), and (021) crystalline peaks of PVDF, respectively. This confirms the partial crystallization of PVDF units in the copolymer and reflects a semicrystalline structure of the PVDF-HFP membrane. A similar pattern was observed when lithium salt was incorporated in the polymer host. With LiTFSI immersed, the diffraction peak intensity of PVDF-HFP is slightly weakened, indicating the amorphous area of PVDF-HFP has increased in LPC. It is quite obvious that another amorphous diffraction peak emerges at ~30° for LPC@UCPBA. This reduction in crystallinity upon the addition of UCPBA is attributed to small particles of fillers that change the chain reorganization around EFI which facilitates ionic conduction (32, 33).

Battery safety is another vital index for the practical application of CPEs (34). Given this, the mechanical properties (Young's modulus and tensile strength) of LPC and LPC@UCPBA were characterized to evaluate their capability of suppressing Li dendrites. The results shown in Fig. 2*G* reveal that the calculated Young's modulus (389 MPa) and tensile strength (20 MPa) of LPC@UCPBA are 41 and 15 times larger than those of LPC, respectively. This significant improvement is due to the strong intermolecular dipole interaction between fillers and polymer matrix, which can afford superior resistance even under violent force, thereby preventing lithium dendrite penetration. Subsequently, the flammability test was conducted to evaluate the fire-resistant property of CPEs (Fig. 2*H*). The filler-free LPC burns out rapidly in less than 5 s, while the LPC@UCPBA shows a sustained flame retardant ability in a burning time of 10 s. The improved mechanical and fire-resistant behavior of LPC@UCPBA is crucial for the safety of solid-state lithium metal batteries.

The approach used in preparing LPC@UCPBA can be generalized to synthesize a series of CPEs with different concentrations of fillers (Fig. 3*A*). To examine the effect of filler concentration on ionic conductivity, a series of quantitative UCPBA (1 wt%, 2 wt%, 5 wt%, and 8 wt%) were added. RT ionic conductivities of these CPEs were determined using electrochemical impedance spectroscopy, and the corresponding Nyquist plots are shown in Fig. 3*B*. The RT ionic conductivity of LPC@2%UCPBA is determined as 0.36 mS cm^{-1}, which is approximately three times that of filler-free LPC. With increasing filler concentration, the RT ionic conductivities of CPEs undergo a slightly decreasing trend from 1.01×10^{-4} S cm^{-1} (LPC@5%UCPBA) to 0.95×10^{-4} S cm^{-1} (LPC@8%UCPBA), which could be caused by aggregation or uneven distribution of UCPBA fillers (*SI Appendix*, Fig. S11). To confirm that the improved RT ionic conductivity of LPC@2%UCPBA is mainly contributed by the construction of a stable EFI, LPC@2%SCPBA (equal mass ratio of LPC with SCPBA) membrane with the same filler concentration was fabricated. It is shown that the ionic resistance of LPC@2%SCPBA is as high as 325 Ω cm^2 (~13 times that of LPC@2%UCPBA), exhibiting a low RT ionic conductivity of 0.29×10^{-4} S cm^{-1} as expected. This result is consistent with the DFT results that a stable electrolyte/filler interfacial interaction is beneficial for the improvement of ion-transport efficiency. The CPEs exhibit temperature-dependent conductivities with typical Arrhenius-like behavior, and the calculated activation energies (E_a) are in the range of 0.24 to 0.33 eV as shown in Fig. 3 *C* and *D* (35). The lowest E_a of LPC@2%UCPBA (0.24 eV) further confirms its low energy barrier for ions hopping between adjacent available sites, which benefits from the robust and successive EFI. The t_{Li}^+ is another important parameter for evaluating the mobility of Li^+ in the CPEs. The CPE with high t_{Li}^+ is beneficial to promote the migration of free Li^+, which reduces the concentration polarization of cations/anions in the EFI and electrolyte/electrode interface (36). Here, the LPC@2%UCPBA shows a higher t_{Li}^+ of 0.6 in contrast to the LPC (0.42) and the LPC@2%SCPBA (0.27) (*SI Appendix*, Fig. S12) since $TFSI^-$ is effectively immobilized by UCPBA, enabling the Li^+ to dominate the ion transport (Fig. 3*E*). Therefore, the kinetic features of ionic migration exhibit good competitiveness with previously reported literature (Fig. 3*F*) (37–41). The local environment of LiTFSI among CPEs is well-investigated through solid-state NMR (ssNMR) spectra, as shown in Fig. 3*G*. When cations are in a strongly bound state, for example, in the LPC@2%SCPBA, it appears as a broad resonance because of the poor mobility. Notably, the ^{7}Li full-width at half-maximum in LPC@2%UCPBA is as low as 130.3 Hz, much lower than that of LPC@2%SCPBA (202.3 Hz). The faster T_2 spin–spin relaxation indicates a much faster motion of free Li^+ in LPC@2%UCPBA (42). In addition, we noticed that the ^{7}Li signal in LPC@2%UCPBA (−1.34 ppm) is downfield shifted compared to that of LPC (−1.56 ppm). Such a downfield shift generally means a reduced electron cloud around the nucleus, highlighting the dissociation of the cations from anions at the stable EFI (Fig. 3*H*) (43).

After understanding interfacial chemistry in different CPEs, other electrochemical properties were also investigated. The high voltage stability of LPC and LPC@2%UCPBA was tested by linear sweep voltammetry (LSV) in Li//stainless-steel (SS) asymmetric cells. As shown in Fig. 4*A*, the LPC@2%UCPBA starts to be oxidized at over ~4.7 V, while the LPC counterpart shows a sharp oxidizing peak starting at ~4.4 V. In addition, when applying a 4.7 V polarization voltage for 24 h on a Li/LPC@2%UCPBA/SS cell at RT, the impedance does not show any obvious increase, indicating a high antioxidative capability of LPC@2%UCPBA (*SI Appendix*, Fig. S13). To investigate the lithium reversibility with different CPEs, a cyclic voltammetry (CV) test in Li//SS cells was carried out between a voltage range of 3.0 to −0.1 V (44). Obvious asymmetric Li-plating/stripping curves were observed for Li/LPC/SS, indicating poor reversibility of lithium in LPC (Fig. 4*B*). After CV tests, its impedance increased significantly with large semicycles, which can be attributed to the irreversible interfacial reaction of Li-metal and LPC (Fig. 4*C*). In contrast, the Li/LPC@2%UCPBA/SS cell presents sharp and symmetric lithium plating (0 → −0.1 V) and stripping (0 → 0.1 V) curves, indicating a high lithium plating/stripping efficiency. In addition, the impedance of the cell does not show a significant increase after the CV test, indicating the formation of a stable interface between lithium and LPC@2%UCPBA. It should be noted that since N,N-dimethylformamide (DMF) was employed as the solvent to prepare the CPEs membranes, a trace amount of residual DMF

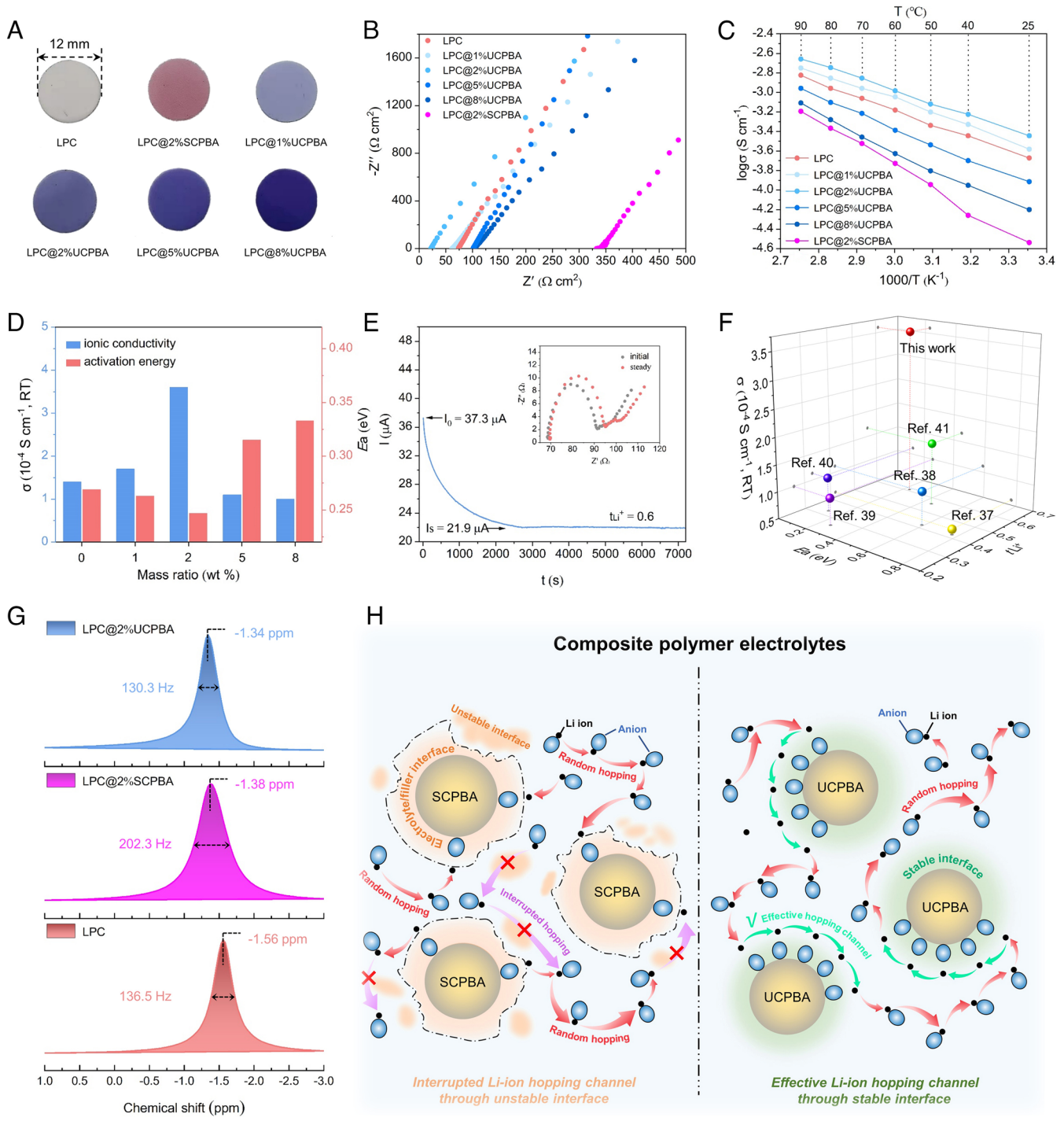

Fig. 3. Electrochemical and physical characterization of the LPC, LPC@SCPBA, and LPC@UCPBA membrane electrolytes. (*A*) Optical photographs of LPC, LPC@2%SCPBA, and LPC@UCPBA with different filler concentrations. (*B*) Nyquist plots of membrane electrolytes at RT. (*C*) Arrhenius plots of membrane electrolytes at different temperatures. (*D*) Comparison of RT ionic conductivity and E_a toward membrane electrolytes. (*E*) Current evolution of Li//Li cell using LPC@2%UCPBA electrolyte under a polarization voltage of 10 mV and the related Nyquist plots before and after testing. (*F*) Comparison of the key properties of LPC@2%UCPBA electrolyte, including σ, E_a, and t_{Li^+} with those reported in the literature. (*G*) ^{7}Li ssNMR spectra of LPC, LPC@2%SCPBA, and LPC@2%UCPBA. (*H*) Illustration of the relationship between EFI stability and Li^+transport efficiency in CPEs. The light blue background represents polymer matrix.

remains in LPC@2%UCPBA owing to the coordination between DMF and Li^+ (45). The thermal gravimetric analysis (TGA) showed a residual DMF content of around 3~5 wt% (*SI Appendix*, Fig. S14). Fortunately, the complex of [Li^+(DMF)$_n$] has been proven to be positive for improving ionic conductivity in polymer-based electrolytes because of an easier movement of small DMF molecules compared with large polymer chains (46). So, trace DMF coordinated with Li^+ also contributes to the electrochemical improvement in LPC@2%UCPBA.

The interfacial stability and dendrite suppression capability of LPC@2%UCPBA were also evaluated in Li//Li symmetric cells. Stable voltage profiles of lithium plating/stripping are observed for Li/LPC@2%UCPBA/Li cell with an overpotential of ~30 mV at 0.1 mA cm^{-2} (Fig. 4*D*). After a super-long time cycling for 4,000 h, the cell only shows a tiny polarization potential rise of ~20 mV. In addition, the constant polarization potential of ~90 mV can be maintained for more than 153 h at a higher current density of 0.5 mA cm^{-2} at RT (*SI Appendix*, Fig. S15), indicating

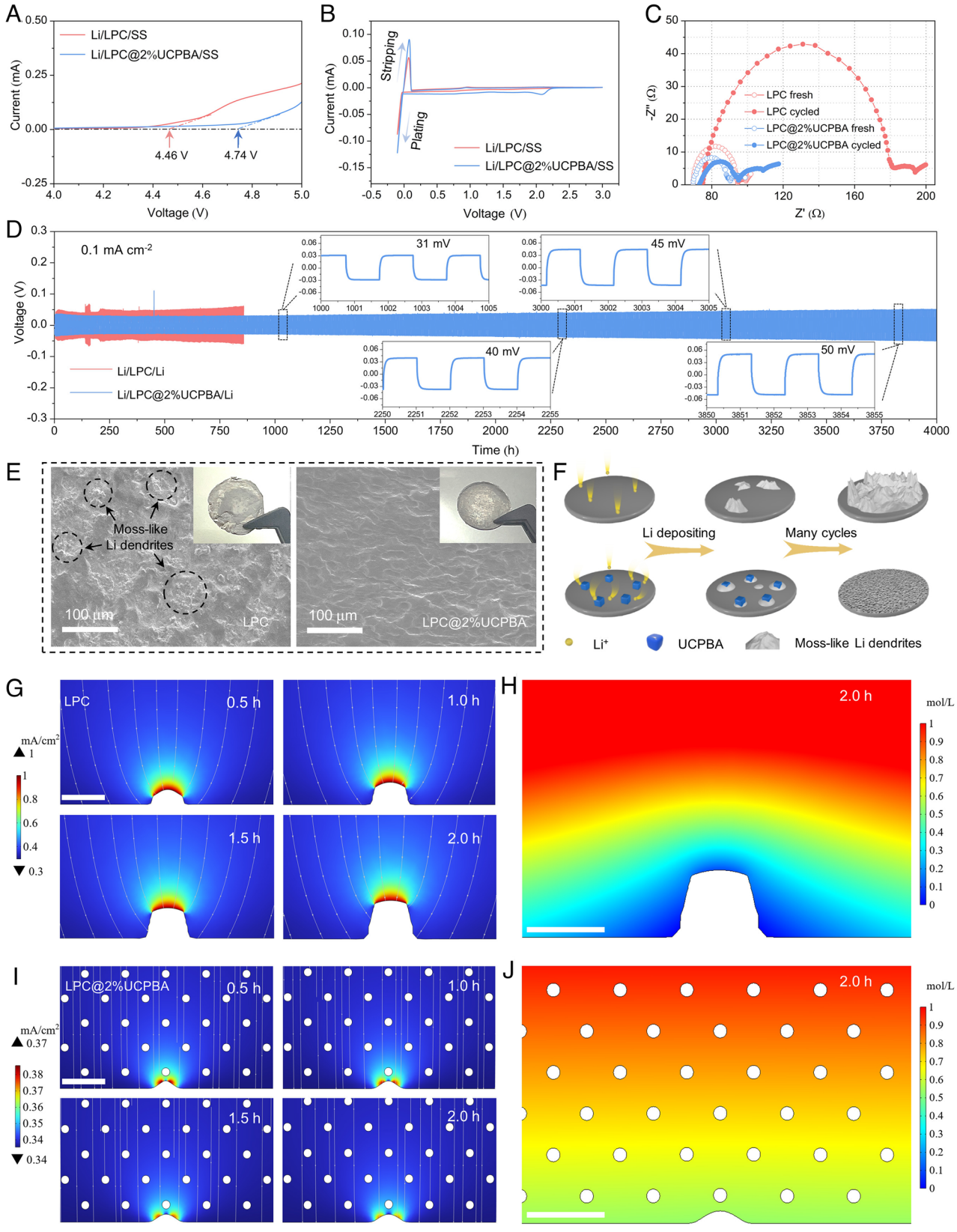

Fig. 4. Electrochemical characterization of Li asymmetrical/symmetrical cells using LPC and LPC@2%UCPBA electrolytes at RT. (*A*) LSV curves of Li//SS cells with a scan rate of 1 mV s^{-1}. (*B*) CV curves of Li//SS cells with a sweep rate of 0.2 mV s^{-1}. (*C*) Nyquist plots of Li//SS cells before and after CV testing. (*D*) Long-term cycling performance of Li//Li symmetrical cells under a current density of 0.1 mA cm^{-2} (zoomed-in plot shown in the *Insets*). (*E*) *Top*-view SEM images and corresponding optical photographs (*Insets*) of cycled Li//Li symmetrical cells. (*F*) Illustration of the mechanism of UCPBA fillers induced homogeneous lithium deposition. (*G–J*) COMSOL Multiphysics simulations of Li-metal deposition and corresponding Li^+ concentration field near the anode substrate in (*G* and *H*) LPC and (*I* and *J*) LPC@2%UCPBA electrolytes. The color in each simulation snapshot indicates the magnitude of spatial Li^+ flux, and the streamlines show the direction of the Li^+ flux. Li-metal is located at the *Bottom*, and the white circles represent UCPBA fillers. (The scale bars are 1 μm.)

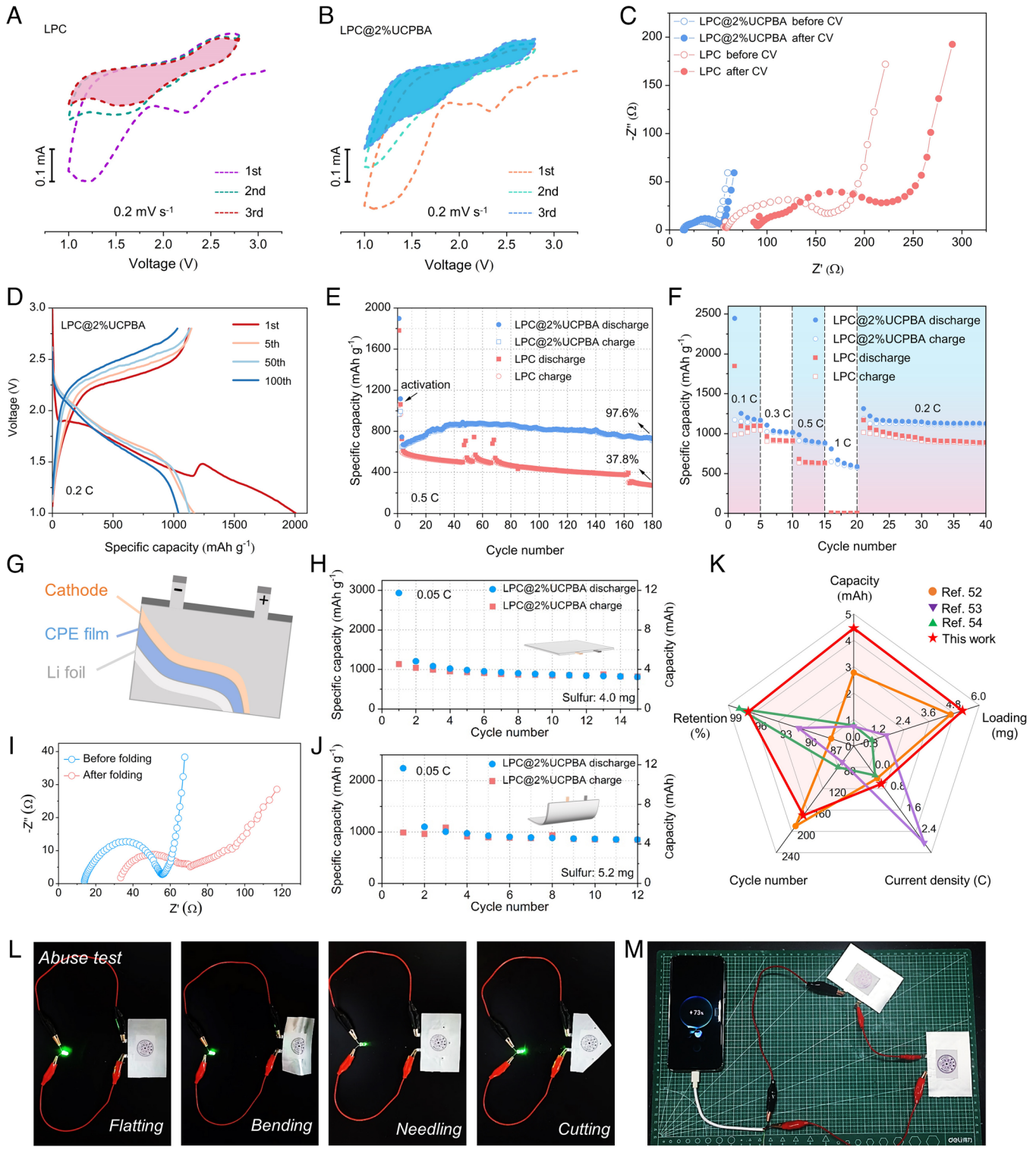

Fig. 5. Performance of Li//SPAN coin cells using LPC and LPC@2%UCPBA electrolytes at RT. (*A* and *B*) CV curves of Li//SPAN cells with a sweep rate of 0.2 mV s^{-1}. (*C*) Nyquist plots of Li//SPAN cells before and after CV testing. (*D*) Charge/discharge voltage profiles of Li/LPC@2%UCPBA/SPAN cell at different cycles. (*E*) Cycling performance of Li//SPAN cells at 0.5 C. (*F*) Specific capacity of Li//SPAN cells at different rates. (*G*) Illustration of Li/LPC@2%UCPBA/SPAN pouch cell. (*H*) Cycling performance of Li/LPC@2%UCPBA/SPAN pouch cell at 0.05 C. (*I*) Nyquist plots of Li/LPC@2%UCPBA/SPAN pouch cell before and after folding test. (*J*) Cycling performance of bent Li/LPC@2%UCPBA/SPAN pouch cell at 0.05 C. (*K*) Performance comparison in terms of capacity, retention, cycle number, current density, and sulfur loading between this work and other literature. (*L*) Abuse tests of Li/LPC@2%UCPBA/SPAN pouch cell lighting a light-emitting diode bulb, which is in flatting, bending, needing, and cutting states. (*M*) Practical test of Li//SPAN pouch cell charging a commercial mobile phone. For coin cells, the areal sulfur loading is 0.5 mg cm^{-2}.

a highly stable interface between lithium and LPC@2%UCPBA, which enables the homogeneous deposition of lithium thus effectively inhibiting the growth of Li dendrites. In comparison, the Li/LPC/Li cell can only cycle for less than 850 h with an amplified overpotential of 60 mV at 0.1 mA cm^{-2}, which exhibits poor interfacial stability with lithium (Fig. 4*D* and *SI Appendix*, Fig. S16). This is strongly confirmed by the top-view SEM images of cycled lithium (Fig. 4*E*). Many moss-like Li dendrites are

observed, which can be attributed to the disordered lithium deposition in different orientations and a continuous accumulation during repeated charge–discharge cycling (47). In sharp contrast, the lithium anode in Li/LPC@2%UCPBA/Li shows a smooth surface with no obvious dendrites after 4,000 h of plating/stripping. The stabilization of the interface and suppression of dendrite growth can be attributed to the stable electrolyte/UCPBA interfaces which act as nanofluidic channels to induce homogeneous Li^+ deposition (Fig. 4*F*). The advantage of UCPBA filler is further verified by the COMSOL Multiphysics simulation (*SI Appendix*, Fig. S17), which models the change in lithium deposition morphology and gradient of interfacial ion concentration distribution (Fig. 4 *G*–*J*). The simulation results show that upon deposition of lithium in the electrolyte without UCPBA, lithium dendrite quickly grows from the random sites of the lithium surface with gathered local current density at the tip of the dendrite (Fig. 4*G*). The inhomogeneous ionic concentration distribution subsequently induces the continuous growth of dendrite (Fig. 4*H*). With the addition of UCPBA, the lithium deposition is found to remain uniform even after two hours of simulation, which is because accelerated Li^+ conduction helps fast supplement lithium and homogenize Li^+ flux at the interface. Importantly, even if the dendrite is generated, the highest current density gradually spreads from the top of the dendrite, which also ensures homogeneous and continuous ionic flux (Fig. 4 *I* and *J*) (48, 49). The simulation details are also vividly displayed in Movies S1 and S2.

As one of the high-energy sulfur-containing cathode materials with both large capacity and long cycling life, SPAN is adopted to investigate the electrochemical performance of LPC@2%UCPBA electrolyte in solid-state Li//SPAN cell (*SI Appendix*, Fig. S18). To enable the Li^+ transport among SPAN particles on the cathode film, the mixture of PVDF-HFP and LiTFSI with a mass ratio of 1:1 was used as the cathode binder. Same as the previous preparation process of electrolyte membranes, DMF was employed as the solvent to prepare the slurry. The CV profiles of Li/LPC/SPAN and Li/LPC@2%UCPBA/SPAN cells at the voltage range of 1.0 to 2.8 V were compared in Fig. 5 *A* and *B*. Both Li//SPAN cells show typical cathodic peaks at around 2.0 V in the first cycles, corresponding to irreversible Li^+ insertion into polymer chain segments of SPAN, which has been proven to be beneficial for enhancing the electrical conductivity of SPAN (50). It is worth noting that the Li/LPC/SPAN cell shows a remarkable increase in interfacial resistance after the CV tests, indicating serious interfacial side reactions and thus gradually degraded interfacial contact (Fig. 5*C*). However, the Li/LPC@2%UCPBA/SPAN cell can afford a barely changed interfacial resistance in sharp contrast with Li/LPC/SPAN cell, which is a result of the improved electrochemical reaction kinetics of Li^+ between electrodes and electrolytes. The galvanostatic discharge–charge curves of the Li/LPC@2%UCPBA/SPAN cell in the initial 100 cycles at the current density of 0.2 C are shown in Fig. 5*D*. The short voltage plateau located at ~2.0 V only appearing in the first discharge curve is associated with the interaction between Li^+ and C=N sites of SPAN, which is consistent with the CV results (51). Subsequently, a sloping curve is observed with a tiny voltage uplift at around 1.3 V in both Li//SPAN cells (*SI Appendix*, Fig. S19), which is likely caused by the residual DMF inducing an enhanced lithiation reaction kinetics of SPAN. In the case of Li/LPC@2%UCPBA/SPAN cell, the discharge–charge curves of the following cycles are substantially overlapped with negligible hysteresis aggravation, indicating superior electrochemical reversibility compared with Li/LPC/SPAN cell.

The cyclability of Li//SPAN cells at 0.2 C and 0.5 C were carried out. The Li/LPC@2%UCPBA/SPAN cell delivers a reversible specific discharge capacity of 1,039 mAh g^{-1} at the 100th cycle at 0.2 C, which is higher than that of Li/LPC/SPAN cell (862 mAh g^{-1}), indicating an enhanced sulfur utilization (*SI Appendix*, Fig. S20). In particular, better cyclability and higher capacity retention of 97.6% after 180 cycles at 0.5 C can be obtained for the Li/LPC@2%UCPBA/SPAN cell, demonstrating its superior cycling stability over the Li/LPC/SPAN cell (Fig. 5*E*). The improved cycling performance is mainly due to the excellent ionic conductivity and t_{Li}^+ with the addition of advanced UCPBA fillers and the intimate interfacial contact between CPE and active materials. The rate capabilities of Li//SPAN cells were evaluated through multirate cycling (Fig. 5*F*). In terms of the Li/LPC/SPAN, it suffers from a serious capacity degradation with the increase of current rate, resulting in a low specific capacity of ~20 mAh g^{-1} at a high current density of 1 C. In contrast, the Li/LPC@2%UCPBA/SPAN cell exhibits a remarkable rate performance with a high specific capacity of ~600 mAh g^{-1} at 1 C. More importantly, the capacity can be recovered to ~1,200 mAh g^{-1} when the current density is switched back to 0.2 C, indicating its good electrochemical reversibility. Overall, these results reveal that the CPE with ligand-modified UCPBA fillers enables significant improvements in both the cyclability and rate capability of solid-state LSBs.

In order to demonstrate the superiority of LPC@2%UCPBA in a more practical regime, pouch cells with high sulfur-loading cathodes were fabricated, as shown in Fig. 5*G*. The pouch cell delivers a high initial capacity of 12 mAh with a sulfur loading of 4.0 mg (Fig. 5*H*). After working at a current density of 0.05 C for 15 cycles, the reversible capacity stabilizes at ~3.3 mAh (*SI Appendix*, Fig. S21). Furthermore, the strong mechanical toughness of LPC@2%UCPBA enables it to remain operational in a bending state as shown in *SI Appendix*, Fig. S22. The interfacial resistance is barely influenced with a slight increase after bending (Fig. 5*I*), indicating high flexibility of LPC@2%UCPBA and stable electrolyte/electrode interface in solid-state LSBs. Given this, raised sulfur loading of 5.2 mg was also exploited. As expected, the bent pouch cell delivers a comparable reversible capacity of ~4.2 mAh after 12 cycles with the reported literature (Fig. 5 *J* and *K* and *SI Appendix*, Fig. S23) (52–54). Furthermore, the pouch cell can operate at various abuse test states, including needling or cutting, and can charge for a commercial mobile phone, demonstrating its excellent practicality (Fig. 5 *L* and *M*). In general, the LPC@2%UCPBA displays advanced flexibility and safety as well as great potential to be applied in solid-state pouch-type LSBs.

Conclusion

In this work, ligand-modified UCPBA filler is designed to improve EFI stability in CPEs. The critical role of interfacial stability has been unraveled by both theoretical and experimental results. Compatible interfaces between UCPBA and LiTFSI and $TFSI^-$ anion absorption on them promote the dissociation of Li^+ from LiTFSI and Li^+ diffusion through the EFI. As a result, in comparison to the filler-free electrolyte, the proposed LPC@2%UCPBA flexible membrane exhibits high RT ionic conductivity of 0.36 mS cm^{-1}, high Li^+ transference number of 0.6, and a wide electrochemical window to 4.74 V. Thus, the proposed strategy to improve EFI stability through ligand modification represents a promising route in constructing a flexible CPE for safe, robust, and high-performance rechargeable solid-state LSBs.

Materials and Methods

Materials Preparation.

Preparation of SCPBA, UCPBA, SCPBA@LiTFSI composites, and UCPBA@LiTFSI composites. All reagents and chemicals were purchased from Sigma-Aldrich without any purification before use. The SCPBA was synthesized via a coprecipitation method. Then, 74.8 mg of $Co(CH_3COO)_2{\cdot}4H_2O$ (99.5%) was dissolved in 40 mL of deionized water under stirring for 1 h (solution A). In addition, 66.4 mg

of $K_3[Co(CN)_6]$ (99%) and 0.5 g of polyvinylpyrrolidone (M.w. ~ 40,000, K30) were dissolved in 60 mL of deionized water under stirring for 1 h (solution B). Solution A was added dropwise to solution B, and the reaction process was kept at room temperature under agitated stirring for 4 h. Then, the pink precipitate (i.e., $Co_3[Co(CN)_6]_2{\cdot}12H_2O$) was collected out and washed with deionized water three times denominated as SCPBA. Followed by thermal dehydration treatment of SCPBA under a vacuum condition at 100 °C for 2 h, the UCPBA sample was achieved. The corresponding composites were prepared by soaking a certain amount of SCPBA or UCPBA into 1 mL 0.1 M LiTFSI/ DMF (anhydrous, 99.8%) solution for 24 h. Then, the solution was heated overnight at 80 °C under a vacuum condition and the SCPBA@LiTFSI or UCPBA@LiTFSI composites were obtained.

Preparation of LPC, LPC@SCPBA, and LPC@UCPBA. The solid-state electrolyte was prepared through a solution-casting method. Here, 0.4 g of PVDF-HFP (M.w. ~ 400,000) and 0.4 g of LiTFSI were mixed in 3 mL of DMF solution, followed by stirring at 80 °C for 4 h. Then, the mixed solution was cast onto a glass substrate using a doctor blade, and the DMF solution was evaporated at 60 °C for 4 h to obtain the LPC sample. The LPC@SCPBA and LPC@UCPBA samples can be achieved when a certain amount of SCPBA or UCPBA is added before the casting process with other conditions unchanged.

Preparation of sulfur-containing cathodes. The SPAN composite was prepared by heating the ball-milled mixture of polyacrylonitrile (M.w. ~ 85,000) and sublimed sulfur in a given weight ratio at 300 °C under an argon atmosphere for 6 h. The cathode slurry was firstly prepared by heat-dissolving 0.2 g of PVDF-HFP and 0.2 g of LiTFSI in 5 mL DMF solution at 80 °C for 4 h. Then, 0.4 g of SPAN and 0.2 g of multiwalled carbon nanotubes (>95%) were mixed into the slurry. The electrodes were prepared by coating the slurry onto an Al foil and dried at 60 °C for 12 h. The average sulfur loading of SPAN cathodes was calculated to be ~0.5 mg cm^{-2}. All the preparation processes were carried out in an Ar-filled glove box.

Materials Characterization. The morphology of materials was characterized by SEM (LEO 1530) with an energy-dispersive spectrometer. XRD (Bruker AXS D8), TGA (TA instruments Q500), and ATR-FTIR (Thermo Nicolet Avatar 320 Spectrometer) spectra were employed for analysis of the crystal structures and composition of the samples. The mechanical performance was tested by a film stress measurement system (FSM 500TC-R). Co *K*-edge XANES measurements and EXAFS analyzation were performed at Canadian Light Source (CLS), using the soft X-ray Micro-characterization beamline (SXRMB, 06B1-1). The STXM and Co *L*-edge measurements were conducted using the SXRMB (10ID-1). The ^{7}Li ssNMR spectra of samples were recorded on a 500 MHz Bruker AVANCE NEO spectrometer equipped with an 11.70 T wide-bore magnet using a 2.5-mm Bruker MAS probe (DVT design) at 25 kHz MAS.

Electrochemical Measurements. For coin cells (CR2032-type), the as-prepared LPC, LPC@SCPBA, and LPC@UCPBA membranes were cut into disks with different diameters and used as the solid-state electrolyte. Symmetric cells of SS/CPE/SS were used to test ionic conductivity according to the equation of

$$\sigma = \frac{L}{(R * S)},$$

where *L*, *R,* and *S* are the thickness, bulk resistance, and area of solid-state electrolyte, respectively, with a Biologic multichannel electrochemical workstation over the frequency range of 0.1 to 10^5 Hz and the AC amplitude of 5 mV. The CPE was cut into a disk with a diameter of 12 mm for the ionic conductivity test. The E_a was calculated according to the Arrhenius equation of

$$K = Ae^{\frac{-Ea}{RT}},$$

where *K* is rate constant, *A* is preexponential factor, *R* is gas constant, and *T* is absolute temperature. The LSV test was determined by employing a Li/CPE/SS model from 3.0 to 5.0 V at a scan rate of 1 mV s^{-1}. CV of Li/CPE/SS asymmetric cells was performed on an electrochemical workstation over the potential range of −0.1 to 3.0 V with a scan rate of 0.2 mV s^{-1}. CV of Li/CPE/SPAN full cells was performed on an electrochemical workstation over the potential range of 1.0 to 2.8 V with a scan rate of 0.2 mV s^{-1}.

A lithium metal tablet was used as both cathode and anode in Li//Li symmetric cells. t_{Li}^+ was measured by combining an AC impedance measurement and a potentiostatic polarization measurement with Li/CPE/Li cells. The t_{Li}^+ was calculated according to the equation:

$$t_{Li^+} = \frac{I_S(\Delta V - I_0R_0)}{I_0(\Delta V - I_SR_s)},$$

where ΔV is the DC polarization voltage (10 mV), I_0 and I_s are initial and stable currents (μA) during polarization, R_0 and R_s are the impedance (Ω) before and after polarization.

A LAND CT2003A electrochemical testing system was used to measure the electrochemical performance of symmetrical and coin cells at room temperature. The CPE was cut into a disk with a diameter of 19 mm for tests. The performance of lithium metal batteries with SPAN as cathode was tested with the voltage range from 1.0 to 2.8 V.

The pouch cells were similarly assembled with lithium metal foil (thickness of 50 μm), CPE, and SPAN electrode inside the glove box. The prepared CPE was closely attached to the SPAN electrode and followed by a physical pressing process onto the lithium metal foil. Al and Ni metal tabs were simultaneously heat-sealed into the pouch cell using Al compound packing film. The sulfur loading of cathodes can reach up to 4.0 ~ 5.2 mg.

DFT Calculations. All of the first-principle calculations were performed based on spin-polarized DFT by Vienna Ab-initio Simulation Package using a Perdew–Burke–Ernzerhof exchange-correlation function under generalized gradient approximation. The electron–ion interaction was considered in the projector-augmented wave method with a plane wave up to an energy of 500 eV. The bulk PBA and PBA (001) surfaces were optimized using Monkhorst-Pack with the conditions of Fermi smearing and a broadening of 0.01 eV, with k-point grids of 2 × 2 × 2 and 1 × 2 × 1, respectively. The atomic relaxation was continued until both the force acting on the atoms was smaller than 0.01 eV $Å^{-1}$ and the energy was converged to 1 × 10^{-5} eV at the same time. The adsorption energies (ΔE_{ads}) were calculated using the following formula:

$$\Delta E_{ads} = E_{surface+ads} - E_{surface} - E_{ads},$$

where $E_{surface+ads}$ is the total energy of the system that LiTFSI species adsorbed on UCPBA (001) surface, $E_{surface}$ is the energy of the clean UCPBA (001) surface, and E_{ads} is the DFT energy of LiTFSI species.

Finite Element Method Simulations. The finite element method based on COMSOL Multiphysics 6.0 was used to simulate the behavior of lithium electrodeposition. Coupled with the tertiary current distribution module and deformed geometry module, the following are the main calculations of the governing equations.

In the solid-state electrolyte, the transfer of Li^+ is governed by the Nernst–Planck equation:

$$N_{Li^+} = -D_{Li^+}(\nabla c_0 - \frac{zFc_0}{RT}\nabla\Phi),$$

where N_{Li}^+ is Li^+ flux, D_{Li}^+ is the diffusion coefficient of Li^+, *z* is the charge of Li^+, c_0 is the concentration of Li^+, *F* is the Faraday's constant, *R* is the ideal gas constant, *T* is the Kelvin temperature, and Φ is the electrolyte potential. Li^+ in the electrolyte follows the equation of conservation of mass and charge:

$$\frac{\partial c_{Li^+}}{\partial t} + \nabla \times N_{Li^+} = 0,$$

$$\sum_i z_i c_i = 0,$$

where c_i is the concentration and z_i is the valence of each species in the electrolyte.

At the interface of the electrolyte and the anode, the deposition process of Li^+ can be described by the simplified reaction:

$$Li^+ + e^+ \leftrightarrow Li,$$

The rate of the Li^+ deposition can be expressed by the local current density, which is given by the Butter–Volmer equation:

$$i = i_0\left[\exp\left(\frac{\alpha_a F\eta}{RT}\right) - \frac{c_{Li+}}{c_0}\exp\left(\frac{\alpha_c F\eta}{RT}\right)\right],$$

where i_0 is exchange current density, η is overpotential, α_a and α_c are the anodic and cathodic charge transfer coefficients, respectively, and c_{Li+} is the concentration of Li^+ near the interface.

Therefore, boundary conditions near the substrate can be described as

$$N_{Li^+}\cdot \boldsymbol{n} = -\frac{i_0}{2F}\left[\exp\left(\frac{\alpha_a F\eta}{RT}\right) - \frac{c_{Li+}}{c_0}\exp\left(\frac{\alpha_c F\eta}{RT}\right)\right],$$

where $\boldsymbol{n}$ is the normal vector of the boundary.

The resulting electrodeposition was assumed to occur in the normal direction to the boundary with a velocity v_n:

$$v_n = \frac{i}{\boldsymbol{n}F}\frac{M}{\rho},$$

where M and ρ are the molar mass and density of Li metal, respectively.

To simulate the morphology of lithium deposits, we set the interface between the anode and electrolyte as a free boundary. The plating/stripping thickness of lithium was used as the displacement in the normal direction and can be expressed by

$$v_n = \boldsymbol{n}\frac{dx}{dt}.$$

The diffusion coefficient and transference number of lithium ions in the solid-state-electrolyte are input from experimental measurements. For the LPC@2%UCPBA electrolytes, We defined the electrochemical parameters of the electrolyte as a whole rather than each filler. Both the anodic and cathodic charge transfer coefficients were set as 0.5, the temperature was fixed at 318 K, and the applied current density was 0.3 mA cm^{-2}. To simulate the dendrite growth, we set a defect at the center of the model, and the calculation model size is 5 μm × 3 μm.

Data, Materials, and Software Availability. All study data are included in the article and/or *SI Appendix*.

ACKNOWLEDGMENTS. This work was supported by the National Key Research and Development Program of China (2021YFB2500200), National Natural Science Foundation of China (No. 52072205), Joint Funds of the National Natural Science Foundation of China (U21A20174), Guangdong Innovative and Entrepreneurial Research Team Program (2021ZT09L197), Shenzhen Science and Technology Program (KQTD20210811090112002), the Start-up Funds, the Overseas Research Cooperation Fund of Tsinghua Shenzhen International Graduate School and the Shenzhen Geim Graphene Center, and Natural Sciences and Engineering Research Council of Canada (NSERC). We acknowledge Dr. Y. Hu from SXRMB at the CLS for XAS measurements. We thank Dr. J.W. who helped us with the Scanning Transmission X-ray Microscopy tests on Spectro-Microscopy Beamline at CLS. The CLS is supported by the NSERC, the National Research Council Canada, the Canadian Institutes of Health Research, the Province of Saskatchewan, Western Economic Diversification Canada, and the University of Saskatchewan. Dr. Q.Z. thanks the Postdoctoral Science Foundation of China (Grant No. 2022M711752).

Author affiliations: [a]Tsinghua-Berkeley Shenzhen Institute and Tsinghua Shenzhen International Graduate School, Shenzhen 518055, Guangdong, People's Republic of China; [b]Department of Chemical Engineering, University of Waterloo, Waterloo N2L 3G1, Ontario, Canada; and [c]Canadian Light Source, Saskatoon, SK S7N 2V3, Canada

1. X. Yang, J. Luo, X. Sun, Towards high-performance solid-state Li-S batteries: From fundamental understanding to engineering design. *Chem. Soc. Rev.* **49**, 2140–2195 (2020).
2. G. Zhou, H. Chen, Y. Cui, Formulating energy density for designing practical lithium-sulfur batteries. *Nat. Energy* **7**, 312–319 (2022).
3. Y. Zheng *et al.*, A review of composite solid-state electrolytes for lithium batteries: Fundamentals, key materials and advanced structures. *Chem. Soc. Rev.* **49**, 8790–8839 (2020).
4. C. Li *et al.*, A quasi-intercalation reaction for fast sulfur redox kinetics in solid-state lithium-sulfur batteries. *Energy Environ. Sci.* **15**, 4289–4300 (2022).
5. J. Sheng *et al.*, Crosslinked nanofiber-reinforced solid-state electrolytes with polysulfide fixation effect towards high safety flexible lithium-sulfur batteries. *Adv. Funct. Mater.* **32**, 2203272 (2022).
6. J. Pan, P. Zhao, N. Wang, F. Huang, S. Dou, Research progress in stable interfacial constructions between composite polymer electrolytes and electrodes. *Energy Environ. Sci.* **15**, 2753–2775 (2022).
7. R. Zhao *et al.*, Metal-organic frameworks for solid-state electrolytes. *Energy Environ. Sci.* **13**, 2386–2403 (2020).
8. T. Wei *et al.*, Activated metal-organic frameworks (a-mil-100 (fe)) as fillers in polymer electrolyte for high-performance all-solid-state lithium metal batteries. *Mater. Today Commun.* **31**, 103518 (2022).
9. M. Hong *et al.*, Ultrafast sintering of solid-state electrolytes with volatile fillers. *ACS Energy Lett.* **6**, 3753–3760 (2021).
10. R. Rojaee *et al.*, Highly-cyclable room-temperature phosphorene polymer electrolyte composites for Li metal batteries. *Adv. Funct. Mater.* **30**, 1910749 (2020).
11. T. Wei *et al.*, Metal-organic framework-based solid-state electrolytes for all solid-state lithium metal batteries: A review. *CrystEngComm*. **24**, 5014–5030 (2022).
12. Z. Wang *et al.*, A metal-organic-framework-based electrolyte with nanowetted interfaces for high-energy-density solid-state lithium battery. *Adv. Mater.* **30**, 1704436 (2018).
13. L. Shen *et al.*, Creating lithium-ion electrolytes with biomimetic ionic channels in metal-organic frameworks. *Adv. Mater.* **30**, 1707476 (2018).
14. S. Fischer *et al.*, A metal-organic framework with tetrahedral aluminate sites as a single-ion Li^+ solid electrolyte. *Angew. Chem. Int. Ed. Engl.* **57**, 16683–16687 (2018).
15. Y. Wu *et al.*, Advances and prospects of PVDF based polymer electrolytes. *J. Energy Chem.* **64**, 62–84 (2022).
16. S. Chen *et al.*, Uniform virus-like Co-N-Cs electrocatalyst derived from prussian blue analog for stretchable fiber-shaped Zn-air batteries. *Adv. Funct. Mater.* **30**, 1908945 (2020).
17. Y. Zhu *et al.*, Compact-nanobox engineering of transition metal oxides with enhanced initial coulombic efficiency for lithium-ion battery anodes. *ACS Appl. Mater. Interfaces* **10**, 8955–8964 (2018).
18. Y. Zhu *et al.*, Tucked flower-like SnS_2/Co_3O_4 composite for high-performance anode material in lithium-ion batteries. *Electrochim. Acta* **190**, 843–851 (2016).
19. Y. Zhu *et al.*, Unsaturated coordination polymer frameworks as multifunctional sulfur reservoir for fast and durable lithium-sulfur batteries. *Nano Energy* **79**, 105393 (2021).
20. S. I. Ohkoshi, K. I. Arai, Y. Sato, K. Hashimoto, Humidity-induced magnetization and magnetic pole inversion in a cyano-bridged metal assembly. *Nat. Mater.* **3**, 857–861 (2004).
21. L. Deng *et al.*, Investigation of the prussian blue analog $Co_3[Co(CN)_6]_2$ as an anode material for nonaqueous potassium-ion batteries. *Adv. Mater.* **30**, 1802510 (2018).
22. J. Zhang *et al.*, Origin of synergistic effects in bicomponent cobalt oxide-platinum catalysts for selective hydrogenation reaction. *Nat. Commun.* **10**, 4166 (2019).
23. A. Bordage *et al.*, In situ site-selective transition metal K-edge XAS: A powerful probe of the transformation of mixed-valence compounds. *Phys. Chem. Chem. Phys.* **17**, 17260–17265 (2015).
24. Y. You, X. Yu, Y. Yin, K. W. Nam, Y. G. Guo, Sodium iron hexacyanoferrate with high Na content as a Na-rich cathode material for Na-ion batteries. *Nano Res.* **8**, 117–128 (2015).
25. R. Zhang *et al.*, Grain boundaries modified uniformly-conjoint metal/oxides via binder strategy as efficient bifunctional electrocatalysts. *J. Mater. Chem. A* **7**, 10010–10018 (2019).
26. U. Kokcam-Demir *et al.*, Coordinatively unsaturated metal sites (open metal sites) in metal-organic frameworks: Design and applications. *Chem. Soc. Rev.* **49**, 2751–2798 (2020).
27. M. B. Dixit *et al.*, Nanoscale mapping of extrinsic interfaces in hybrid solid electrolytes. *Joule* **4**, 207–221 (2020).
28. S. Sun *et al.*, Nano-scale spatial assessment of calcium distribution in coccolithophores using synchrotron-based nano-CT and STXM-NEXAFS. *Int. J. Mol. Sci.* **15**, 23604–23615 (2014).
29. P. Zhang *et al.*, Biotransformation of ceria nanoparticles in cucumber plants. *ACS Nano* **6**, 9943–9950 (2012).
30. J. Wang, J. Zhou, Y. Hu, T. Regier, Chemical interaction and imaging of single Co_3O_4/graphene sheets studied by scanning transmission X-ray microscopy and X-ray absorption spectroscopy. *Energy Environ. Sci.* **6**, 926–934 (2013).
31. M. L. Baker *et al.*, K- and L-edge X-ray absorption spectroscopy (XAS) and resonant inelastic X-ray scattering (RIXS) determination of differential orbital covalency (DOC) of transition metal sites. *Coord. Chem. Rev.* **345**, 182–208 (2017).
32. L. Liu *et al.*, Synergistic effect of lithium salts with fillers and solvents in composite electrolytes for superior room-temperature solid-state lithium batteries. *ACS Appl. Energy Mater.* **5**, 2484–2494 (2022).
33. J. Sun *et al.*, Facilitating interfacial stability via bilayer heterostructure solid electrolyte toward high-energy, safe and adaptable lithium batteries. *Adv. Energy Mater.* **10**, 2000709 (2020).
34. K. Liu, Y. Liu, D. Lin, A. Pei, Y. Cui, Materials for lithium-ion battery safety. *Sci. Adv.* **4**, 9820 (2018).
35. Y. Zheng *et al.*, "Tree-Trunk" design for flexible quasi-solid-state electrolytes with hierarchical ion-channels enabling ultralong-life lithium-metal batteries. *Adv. Mater.* **34**, e2203417 (2022).
36. Y. M. Jeon, S. Kim, M. Lee, W. B. Lee, J. H. Park, Polymer-clay nanocomposite solid-state electrolyte with selective cation transport boosting and retarded lithium dendrite formation. *Adv. Energy Mater.* **10**, 2003114 (2020).
37. W. Liu *et al.*, Enhancing ionic conductivity in composite polymer electrolytes with well-aligned ceramic nanowires. *Nat. Energy* **2**, 17035 (2017).
38. S. L. Beshahwured *et al.*, Flexible hybrid solid electrolyte incorporating ligament-shaped $Li_{6.25}Al_{0.25}La_3Zr_2O_{12}$ filler for all-solid-state lithium-metal batteries. *Electrochim. Acta* **366**, 137348 (2021).
39. N. Wu *et al.*, Enhanced surface interactions enable fast Li^+ conduction in oxide/polymer composite electrolyte. *Angew. Chem. Int. Ed. Engl.* **59**, 4131–4137 (2020).
40. T. Yang, J. Zheng, Q. Cheng, Y. Y. Hu, C. K. Chan, Composite polymer electrolytes with $Li_7La_3Zr_2O_{12}$ Garnet-type nanowires as ceramic fillers: Mechanism of conductivity enhancement and role of doping and morphology. *ACS Appl. Mater. Interfaces* **9**, 21773–21780 (2017).

41. X. Wang *et al.*, Rechargeable solid-state lithium metal batteries with vertically aligned ceramic nanoparticle/polymer composite electrolyte. *Nano Energy* **60**, 205–212 (2019).
42. D. Guo *et al.*, Foldable solid-state batteries enabled by electrolyte mediation in covalent organic frameworks. *Adv. Mater.* **34**, 2201410 (2022).
43. C. Yang *et al.*, Copper-coordinated cellulose ion conductors for solid-state batteries. *Nature* **598**, 590–596 (2021).
44. H. Sun *et al.*, Fluorinated poly-oxalate electrolytes stabilizing both anode and cathode interfaces for all-solid-state Li/NMC811 batteries. *Angew. Chem. Int. Ed. Engl.* **60**, 18335–18343 (2021).
45. Q. Liu *et al.*, Polymer electrolytes based on interactions between [solvent-Li^+] complex and solvent-modified polymer. *Energy Storage Mater.* **51**, 443–452 (2022).
46. K. Yang *et al.*, Stable interface chemistry and multiple ion transport of composite electrolyte contribute to ultra-long cycling solid-state $LiNi_{0.8}Co_{0.1}Mn_{0.1}O_2$/lithium metal batteries. *Angew. Chem. Int. Ed. Engl.* **60**, 24668–24675 (2021).
47. T. Mu *et al.*, Interface defect chemistry enables dendrite-free lithium metal anodes. *Chem. Eng. J.* **437**, 135109 (2022).
48. J. Zhou *et al.*, Diminishing interfacial turbulence by colloid-polymer electrolyte to stabilize zinc ion flux for deep-cycling Zn metal batteries. *Adv. Mater.* **34**, 2200131 (2022).
49. J. Zhou *et al.*, New type of dynamically "Solid-Liquid" interconvertible electrolyte for high-rate Zn metal battery. *Nano Lett.* **22**, 2898–2906 (2022).
50. L. Zeng *et al.*, Catalytic effect of electrodes and electrolytes in metal-sulfur batteries: Progress and prospective. *Adv. Mater.* **34**, 2204636 (2022).
51. B. Chen, X. Zhong, G. Zhou, N. Zhao, H. M. Cheng, Graphene-supported atomically dispersed metals as bifunctional catalysts for next-generation batteries based on conversion reactions. *Adv. Mater.* **34**, 2105812 (2022).
52. L. P. Hou *et al.*, Improved interfacial electronic contacts powering high sulfur utilization in all-solid-state lithium-sulfur batteries. *Energy Storage Mater.* **25**, 436–442 (2020).
53. X. Tao *et al.*, Solid-state lithium-sulfur batteries operated at 37 °C with composites of nanostructured $Li_7La_3Zr_2O_{12}$/carbon foam and polymer. *Nano Lett.* **17**, 2967–2972 (2017).
54. L. Chen, L. Z. Fan, Dendrite-free Li metal deposition in all-solid-state lithium sulfur batteries with polymer-in-salt polysiloxane electrolyte. *Energy Storage Mater.* **15**, 37–45 (2018).